Real-space atomic dynamics in metallic liquids investigated by inelastic neutron scattering

Zengquan Wang,[1] Wojciech Dmowski,[1,*] Hui Wang,[1] Robert Ashcraft,[2] Douglas L. Abernathy,[3] Kenneth F. Kelton,[2] and Takeshi Egami[1,4,5,†]

[1]*Shull-Wollan Center, Department of Materials Science and Engineering, University of Tennessee, Knoxville, Tennessee 37996, USA*
[2]*Department of Physics and Institute of Materials Science and Engineering, Washington University, St. Louis, Missouri 63130, USA*
[3]*Neutron Scattering Division, Oak Ridge National Laboratory, Oak Ridge, Tennessee 37831, USA*
[4]*Department of Physics and Astronomy, University of Tennessee, Knoxville, Tennessee 37996, USA*
[5]*Materials Sciences and Technology Division, Oak Ridge National Laboratory, Oak Ridge, Tennessee 37831, USA*

(Received 11 March 2024; revised 23 June 2024; accepted 26 June 2024; published 12 July 2024)

Understanding the dynamics of liquids at the atomic level remains a major challenge. Even though viscosity is one of the most fundamental properties of liquids, its atomistic origin is not fully elucidated. Through inelastic neutron scattering experiment on levitated metallic liquid droplets, the time-dependent pair correlation function, the Van Hove function, was determined for $Zr_{50}Cu_{50}$ and $Zr_{80}Pt_{20}$ liquids at various temperatures. The time for change in local atomic connectivity, τ_{LC}, which is the timescale of atomic bond cutting and forming, is estimated based on the exponential decay of the nearest neighbor peak of the Van Hove function. At high temperatures above the crossover temperature T_A, τ_{LC} is equal to the Maxwell relaxation time, $\tau_M = \eta/G_\infty$, where η is the macroscopic shear viscosity and G_∞ is the high-frequency shear modulus. Below T_A the ratio of τ_M/τ_{LC} increases with decreasing temperature, indicating increased atomic cooperativity as predicted by molecular dynamics simulation.

DOI: 10.1103/PhysRevB.110.024309

I. INTRODUCTION

Amorphous matters, including glasses and liquids, are ubiquitous in nature. However, the science of liquids and glasses is less developed compared to that of crystalline solids, mainly because they lack periodicity in structure whereas most theories in condensed-matter physics assume periodic structures. For example, even though viscosity is one of the most common and fundamental properties of liquids, its atomic mechanism is still not well understood [1–3]. Here, we address this question using inelastic neutron scattering with representation of the results in real space and time.

Angell plotted the viscosity in logarithmic scale vs the inverse temperature reduced by the glass transition temperature T_g and defined the fragility of liquids by the slope of the data at T_g to categorize liquids [4–6]. Strong liquids such as network oxides show Arrhenius behavior, whereas for the relatively fragile liquids, such as most metallic liquids, their viscosities exhibit the Arrhenius behavior at high temperatures and become super-Arrhenius below the crossover temperature T_A. Currently, a major focus of research is on either the supercooled liquid or the glass transition region, trying to understand the nature of the glass transition [1–3,7–9]. The high-temperature behavior of liquids has been assumed to be gaslike and trivial. However, this assumption is highly questionable, because atoms in high-temperature liquids are still strongly bound together and their motions are thermally activated following the Arrhenius law. In fact, the snapshot structures of the supercooled liquids and high-temperature liquids are similar, with only slight differences in the medium-range order [10], even though their dynamics are vastly different. In this work we focus on the evolution of atomic-level dynamics through the crossover from Arrhenius to super-Arrhenius behavior.

Our previous molecular dynamics (MD) simulation results [11] show that the time for the change in local atomic connectivity, τ_{LC}, which is defined as the time for an atom to lose or gain one neighboring atom, is approximately equal to the Maxwell relaxation time τ_M $(= \eta/G_\infty$, where η is macroscopic shear viscosity and G_∞ is the high-frequency shear modulus) in high-temperature metallic liquids. This simulation directly connects the timescale of the microscopic behavior and that of the macroscopic viscous behavior in metallic liquids and shows that the shear viscosity is controlled by the local connectivity change through bond cutting and reforming. Here, atomic bond is defined between the center atom and the nearest neighboring atoms, which are within the first peak of the pair distribution function (PDF). Bond cutting means an atom moves out of the nearest neighboring shell and bond forming means an atom moves into that shell. The results were supported by an inelastic neutron scattering measurement on a $Zr_{80}Pt_{20}$ liquid suspended by electrostatic levitation and analyzed in terms of the Van Hove function (VHF) [12]. In this work we extend the analysis by studying a $Zr_{50}Cu_{50}$ liquid in addition to the $Zr_{80}Pt_{20}$ liquid, focusing on the temperature range around T_A.

The VHF, $G(\boldsymbol{r}, t)$, is the probability to find one particle at position $\boldsymbol{r}$ and time t, given that there was an atom at the

*Contact author: wdmowski@utk.edu
†Contact author: egami@utk.edu

origin and time $t = 0$. It is defined as [13]

$$G(\boldsymbol{r}, t) = \frac{1}{N}\left\langle \sum_{i,j}^{N} \delta[\boldsymbol{r} + \boldsymbol{r}_j(0) - \boldsymbol{r}_i(t)] \right\rangle. \quad (1)$$

It contains the self-part, $G_s(\boldsymbol{r}, t)$ (when $i = j$), which describes the self-diffusion behavior of a single atom, and the distinct part, $G_d(\boldsymbol{r}, t)$ (when $i \neq j$), which describes the cross correlation between different atoms. Through the VHF it is possible to envisage the dynamic two-body correlations among atoms in real space and time. Experimentally it can be determined through the double Fourier transform of the dynamic structure factor, $S(\boldsymbol{Q}, \omega)$,

$$G(\boldsymbol{r}, t) = \frac{1}{(2\pi)^3 \rho} \int S(\boldsymbol{Q}, \omega) \exp[i(\omega t - \boldsymbol{Q} \cdot \boldsymbol{r})] d\omega d\boldsymbol{Q}, \quad (2)$$

where $\boldsymbol{Q}$ is the momentum exchange and $E = \hbar\omega$ is the energy exchange of inelastic scattering. The $S(\boldsymbol{Q}, \omega)$ can be measured by inelastic neutron or x-ray scattering. Note that the VHF function obtained from the experiment is slightly different from the original theoretical definition in Eq. (1). It is normalized by the number density ρ and 1 is subtracted, thus the physical meaning is unchanged. However, for accurate evaluation of the VHF, $S(\boldsymbol{Q}, \omega)$ has to be measured over wide ranges of Q and E. This used to be quite time-consuming with reactor neutron sources. Consequently, only a few attempts have been made in the past [14–16] and the VHF has been studied mostly in molecular dynamics simulations [17–22]. However, recently with the development of more advanced instrumentation [23,24], it became feasible to obtain the Van Hove function more easily through inelastic neutron or x-ray scattering and to experimentally analyze the dynamics in liquids in real space and time [12,25–27].

In this work, the inelastic neutron scattering (INS) technique was applied on metallic liquid droplet samples levitated by an electrostatic levitator [28], and the dynamic structure function $S(Q, \omega)$ was determined at various temperatures. A procedure was developed to reliably obtain the distinct part of the Van Hove function, $G_d(r, t)$, based on the double Fourier transform method. The dynamic relaxation behavior of the first peak of $G_d(r, t)$ confirms experimentally that the shear viscosity of metallic liquids is controlled by the local configurational change at the atomistic level, as predicted by simulation [11].

II. EXPERIMENTAL DETAILS

Measurements of metallic liquid samples at high temperatures were always beleaguered by issues such as the sample-container reaction, contamination, and oxidization. To minimize these issues, liquid samples in this experiment were handled by the technique of electrostatic levitation, providing a containerless and high vacuum processing environment. The inelastic neutron scattering (INS) experiments on the levitated metallic liquids were done at the Wide Angular-Range Chopper Spectrometer (BL-18, ARCS) [29] at the Spallation Neutron Source (SNS) of Oak Ridge National Laboratory (ORNL) with the Neutron Electrostatic Levitator (NESL) installed as sample environment at ARCS [30]. Solid spherical $Zr_{50}Cu_{50}$ and $Zr_{80}Pt_{20}$ samples with a mass of about 300–400 mg and a diameter of about 4–5 mm were levitated and heated by a solid-state laser to the molten state and then held at specified temperatures. The temperature ranges were $T_s - 150$ K to $T_s + 150$ K (1028–1328 K) for $Zr_{50}Cu_{50}$, of which the solidus temperature T_s is 1178 K, and $T_s - 150$ K to $T_s + 360$ K (1303–1813 K) for $Zr_{80}Pt_{20}$, of which T_s is 1453 K. These ranges were chosen by taking into account the degree of supercooling, evaporation of the metallic elements of the samples, and the heating capability of the levitator. The atomic concentration remains unchanged as the negligible evaporation of the elements was further confirmed by the undetectable sample mass change after the experiment. The temperature of the sample was calibrated with the solidus temperature plateau during the levitated melting. The viscosity of the liquid samples within similar temperature ranges are from Ref. [31], measured by an oscillating drop method with a similar levitator. Neutron scattering data were collected for about 2 h at each temperature level with the neutron incident energy E_i of 20 meV. The choice of this incident energy represents a compromise between the energy resolution and Q coverage. The Q coverage was up to 5.74 Å^{-1}, enough to cover the first two main structural scattering peaks. The collected INS time-of-flight (TOF) raw data were reduced to the scattering spectrum $I(Q, E)$ where Q is the momentum transfer and E is the energy transfer, using the standardized direct-geometry spectrometer (DGS) data reduction routine, and the Mslice module in DAVE software [32] and MANTID software [33]. The exact values of source parameters E_i and T_0 used for data reduction were determined from standard white beam calibrations using a vanadium sample. The scattering signal from the empty NESL levitator chamber was also measured for background subtraction, which was as low as three orders of magnitude smaller than the sample scattering at the important spectrum region around the main peaks, demonstrating the advantage of using the containerless environment. Multiple scattering can be neglected as the neutron mean free path in the samples is much larger than the sample size. Scattering power represented by the scattering cross section (sum of coherent and incoherent scattering) for $Zr_{50}Cu_{50}$ alloy is 7.25 barns (10^{-24} cm^2) and for $Zr_{80}Pt_{20}$ alloy 7.51 barns. The incoherent scattering from both samples is significantly lower than the coherent scattering since the incoherent scattering cross sections for Zr, Cu, and Pt are much smaller [Cu: σ_coh = 7.485, σ_inc = 0.55; Zr: σ_coh = 6.44, σ_inc = 0.02; Pt: σ_coh = 11.58, σ_inc = 0.13; all in barns (10^{-24} cm^2)]. The energy resolution was measured and corrected using a vanadium sample at the same E_i, because the neutron scattering from vanadium is mostly incoherent. Then the dynamic structure factor $S(Q, \omega)$ was obtained and the Van Hove function was calculated through the double Fourier transform shown in Eq. (2), using the customized data processing procedure that will be discussed in detail in Sec. III A.

III. DATA ANALYSIS AND RESULTS

A. Obtaining the Van Hove function $G(r, t)$

The Van Hove function $G(r, t)$ is defined by Eq. (1), and can be calculated from MD simulation trajectories, but experimentally it is determined from inelastic scattering data

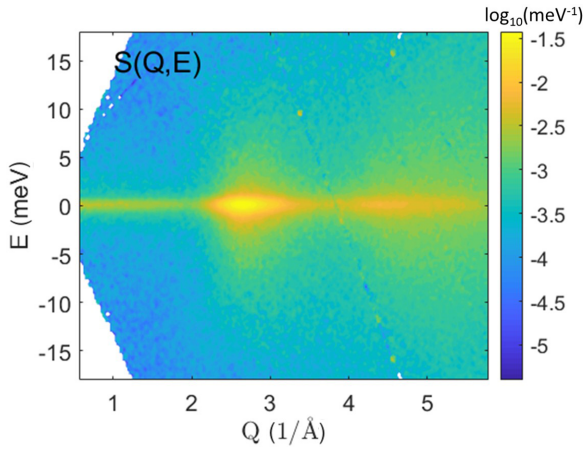

FIG. 1. Dynamic structure factor $S(Q, E)$ obtained for levitated $Zr_{50}Cu_{50}$ liquid through INS measurement after applying background subtraction, detailed balance correction, and interpolation. The color bar shows the logarithm of the intensity value. A few distinct spots (bright yellow and dark blue ones) are from the detector array gap or edge due to imperfectness of interpolation. Blank (white) region and spots are inaccessible (Q, E) range and missing data, and are treated as NaN.

based on Eq. (2). The customized procedure is described below.

The $I(Q, E)$ spectrum of neutrons inelastically scattered from the sample is obtained through standard reduction of raw time-of-flight (TOF) inelastic scattering data and appropriate subtraction of the empty levitator background. The detailed balance principle [34] through $I(Q, E) = I(Q, -E)\exp(\hbar\omega/k_BT)$ is used to extend the data range to include the inaccessible positive energy transfer region restricted by the dynamic limitations. By normalizing to the square of the mean neutron scattering length $\langle b\rangle^2$, the dynamic structure function $S(Q, E)$ of the sample is obtained, as shown in Fig 1. Some interpolations have also been made to fill the blank line due to gaps between the detector arrays.

The intermediate scattering function $F(Q, t)$ is determined by the Fourier transform of $S(Q, \omega)$ through $F(Q, t) = \int_{-E_{\max}}^{E_{\max}} S(Q, \omega)\exp(i\omega t)d\omega$. The contour plot and the different time slices are shown in Fig. 2. Conforming to the static structure function $S(Q) = F(Q, t = 0)$ relation, the first maximum of $F(Q, t)$ decays quickly with time and the $t = 0$ slice, $F(Q, t = 0)$, oscillates around a constant value, as Q is large enough. Further normalization of $F(Q, t)$ by this constant value will be applied later after the energy resolution correction to enforce that $S(Q)$ oscillates around unity as $Q \to \infty$. The time dependent relaxation of the first maximum, $F(Q_1, t)$, also known as α relaxation, has been widely used to analyze the structural change of liquids. However, the analysis of the Van Hove function by simulation showed that the α relaxation using reciprocal space information does not provide the true structural change or local dynamics of the liquid system [35], which suggests the importance of real-space investigations.

In typical INS measurements, the scattering intensity from the sample is convoluted with the neutron beam energy resolution function. One way to improve the energy resolution is to use a lower incident energy, but this reduces the accessible range of Q. As a compromise we chose the incident energy of 20 meV. To implement the energy resolution correction, we apply the deconvolution of the beamline energy profile. In TOF INS measurements the energy resolution slightly depends on the transfer energy, but the dependence is weak at low transfer energies where $S(Q, E)$ is most appreciable. Thus, we use the energy resolution of the elastic line for the entire energy range. With the reasonable assumption that vanadium is an almost purely incoherent scatterer, its elastic scattering intensity can be used to determine the neutron energy profile. Hence, the total dynamic structure factor can be expressed as

$$S_{\text{tot}}(Q, E) = S_{\text{sample}}(Q, E) * S_V(Q, E), \tag{3}$$

where S_{tot} is the total dynamic structure factor directly measured from the liquid samples, S_{sample} is the intrinsic dynamic structure factor for the sample, $*$ indicates a convolution operation, and S_V is the dynamic structure factor measured from the standard vanadium sample with the same incident energy at room temperature, which is almost Q independent and represents the beamline geometry and neutron energy profile. By applying the Fourier transform over E or ω to both sides of Eq. (3), the convolution of dynamic structure factors

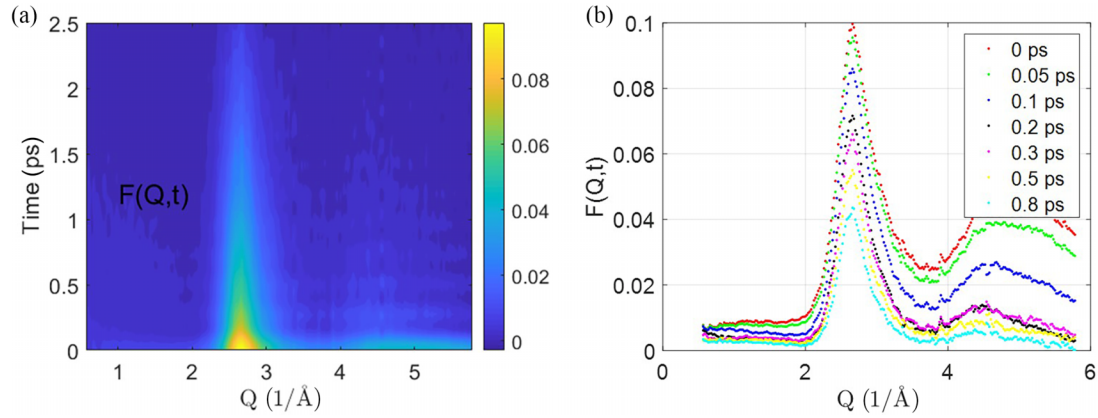

FIG. 2. Intermediate scattering function, $F(Q, t)$, determined through the Fourier transform of $S(Q, \omega)$ without normalization and energy resolution correction: (a) contour plot and (b) slices at specific times.

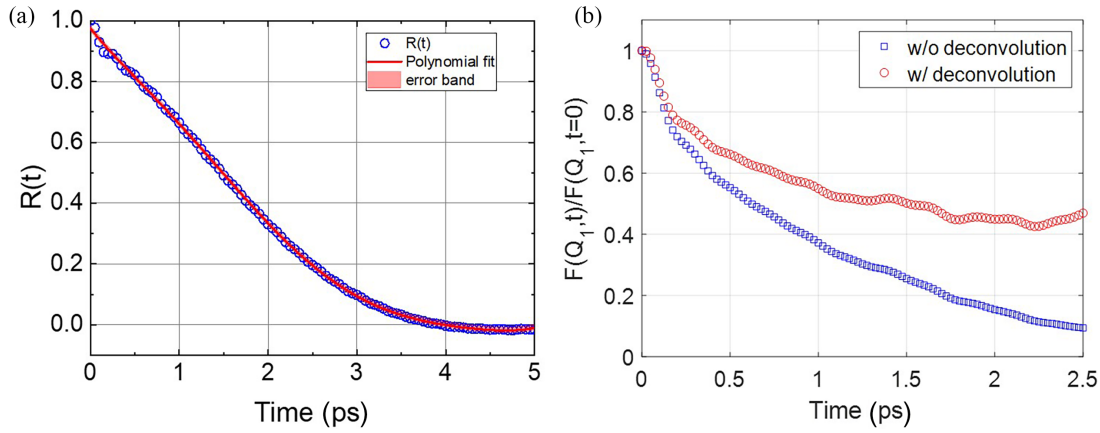

FIG. 3. (a) Energy resolution correction function $R(t)$ measured from vanadium standard for $E_i = 20$ meV at ARCS and its polynomial fitting; (b) comparison of the α relaxation for $Zr_{50}Cu_{50}$ before and after energy resolution correction.

becomes a multiplication of intermediate scattering functions,

$$F_{\text{tot}}(Q, t) = F_{\text{sample}}(Q, t)R(t), \tag{4}$$

where the energy resolution correction function $R(t)$ is the Fourier transform of $S_V(Q, E)$ for $E_i = 20$ meV measured at the ARCS beamline. A six-order polynomial fit was used to obtain a smooth $R(t)$. The portion for $t > 2$ ps is discarded due to an overcorrection at long times, as shown in Fig. 3(a). Then the true intermediate scattering function for the sample can be obtained by

$$F(Q, t) = F_{\text{tot}}(Q, t)/R(t). \tag{5}$$

The effect of the energy resolution correction can be shown by plotting the normalized α relaxation before and after the correction for $Zr_{50}Cu_{50}$ at $T_s + 50$ K, as shown in Fig. 3(b). Before the energy resolution correction (deconvolution), the relaxation is much faster and gives a short relaxation time. After the correction, the α relaxation gives a larger and more accurate and reasonable relaxation time. Although there is some degree of overcorrection for longer times and for samples at lower temperatures, where the relaxation curve becomes too flat, it is still better than using data without the correction.

The self-part of the intermediate scattering function $F_s(Q, t)$ is attributed to the incoherent part of the scattering, thus it can be fitted by the Gaussian approximation for diffusive dynamics, $F_s(Q, t) \approx A(t)\exp[-w(t)Q^2]$, where $A(t)$ and $w(t)$ are the time-dependent amplitude and width function. The $F(Q, t)$ in all t slices can be fitted with the Gaussian curve to separate the self-part, $F_s(Q, t)$, and the distinct part, $F_d(Q, t)$ [$= F(Q, t) - F_s(Q, t)$]. The fitting range is 1.9 Å^{-1} to $Q_{\max}$ (~ 5.8Å^{-1}) for $Zr_{50}Cu_{50}$ and 1.8 Å^{-1} to $Q_{\max}$ for $Zr_{80}Pt_{20}$. Each time slice was carefully checked to make sure that the fitting was reasonably good. Another benefit of the Gaussian fitting is the ability to extrapolate the data to a larger Q range (0–50 Å^{-1}) to avoid termination errors for the second Fourier transform [24]. At $t = 0$, $w(t = 0)$ equals 0 and $F(Q, t = 0)$ oscillates around the constant value $A(t = 0)$ as $Q \to \infty$, justifying the reliability of the first Fourier transform. Both $F_s(Q, t)$ and $F_d(Q, t)$ are then normalized by the $A(t = 0)$ value to enforce that $S(Q)$ oscillates around unity as $Q \to \infty$. The normalized $F(Q, t)$ is similar to Fig. 2 and is not shown here. The self- and distinct parts of $F(Q, t)$ reflect the single particle diffusive dynamics and the collective atomic density fluctuations, and are dominated by the incoherent and coherent neutron scattering, respectively.

Considering the isotropic nature of metallic liquids, $\exp(i\mathbf{Q}\cdot\mathbf{r})$ becomes $4\pi Q^2\sin(Qr)/(Qr)$ after angular integration, and the self- and distinct parts of $G(r, t)$ can be obtained by the subsequent Fourier transformation of the corresponding $F(Q, t)$ over Q. Here we focus on the distinct part, which describes the cross correlation between atoms, and is obtained by

$$G_d(r, t) = \frac{1}{2\pi^2\rho}\int_{Q_{\min}}^{Q_{\max}} F_d(Q, t)\frac{\sin(Qr)}{Qr}Q^2 dQ, \tag{6}$$

where ρ is the atomic number density, which changes less than 2% within the measured temperature range. The damping function $\sin(x)/x$ was applied to the tail of $F_d(Q, t)$ to suppress the truncation error in the Fourier transform. A typical distinct part of the Van Hove function is shown in Fig. 4. Note that the smoothness of the data is due to the strong filtering effect of the double Fourier transformation. When $t = 0$, it can be obtained from Eq. (6) that $G_d(r, 0) = g(r) - 1$, where $g(r)$ is the pair distribution function (PDF) and describes the instantaneous structure of the liquid. However, because the energy range of the measurement, up to 20 meV, does not fully cover the phonons, which extend to over 40 meV, the peaks of $G_d(r, 0)$ are slightly underestimated. Nevertheless, the coordination number calculated from $G_d(r, 0)$ is about 12.8 for $Zr_{50}Cu_{50}$ and 12.9 for $Zr_{80}Pt_{20}$ at all temperatures, which is very close to the expected value of $4\pi = 12.56$ [36], supporting the validity of the data processing procedure and the obtained $G_d(r, t)$ here.

B. Relaxation behavior

To analyze the dynamic relaxation behavior of $G_d(r, t)$, a new parameter $\Delta N_1(t)$ is defined as $\Delta N_1(t) = \int_{r_1}^{r_2} 4\pi r^2\rho_0 G_d(r, t)dr$, where the integration range $[r_1, r_2]$ is the distance range for the part of the first peak where the value of $G_d(r, t)$ is positive. Comparing with the coordination number defined by $N = \int_{r_1}^{r_2} 4\pi r^2\rho_0 g(r)dr$, the $\Delta N_1(t)$

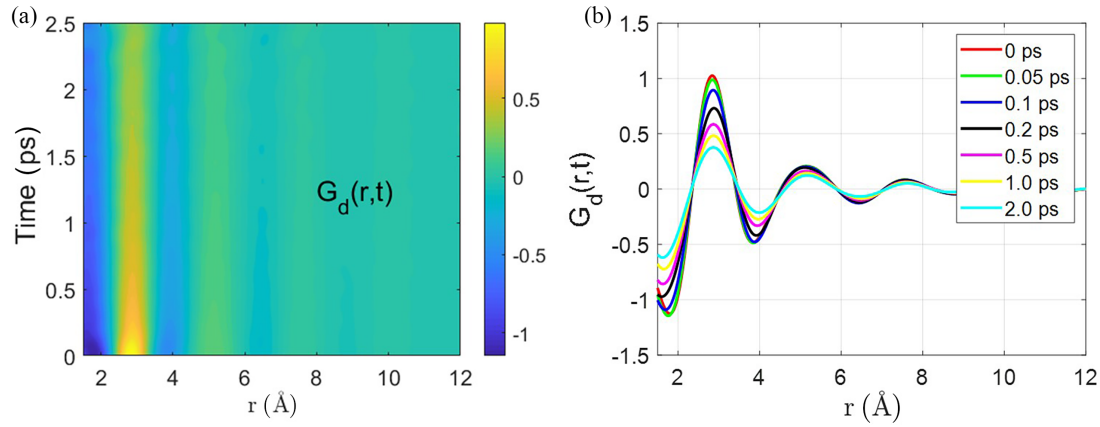

FIG. 4. The distinct part of the Van Hove function $G_d(r, t)$ for $Zr_{50}Cu_{50}$ at $T_s + 50$ K: (a) contour plot and (b) slices at specific times. The smoothness of the data is due to the strong filtering effect of the double Fourier transformation.

represents the part of the PDF first peak for which $g(r) > 1$ and means the excess of the number density in the nearest neighbor shell compared to the long-range average. Its value at $t = 0$ is between 3.7 and 3.9 for $Zr_{50}Cu_{50}$, and between 4.3 and 4.8 for $Zr_{80}Pt_{20}$, with a slight temperature dependence. The evolution of $\Delta N_1(t)$ with time describes how the bulk of the nearest neighboring atoms move away from the atom at the center. Thus, this parameter is chosen to reflect the collective dynamics of atoms moving from and to the nearest neighbor shell, since the first main peak value of $G(r, t)$, corresponding to the average atoms spacing, does not catch all atoms, is affected by temperature, and carries less statistical weight. The $\Delta N_1(t)$ normalized by its value at $t = 0$ is plotted in Fig. 5(a) for $Zr_{50}Cu_{50}$ liquids at different temperatures. As expected, the relaxation slows down as temperature decreases. At least two relaxation modes can be observed for both $Zr_{50}Cu_{50}$ and $Zr_{80}Pt_{20}$ liquids at all different temperatures: a faster relaxation mode when $t < 0.25$ ps, corresponding to part of the fast phononic motion, and a slower one when $t > 0.25$ ps, corresponding to the slower collective motion of atoms, in the metallic liquids.

The two relaxation modes of $\Delta N_1(t)$ at different temperatures can be fitted by a two-part exponential decay function,

$$y(t) = A_1 \exp\left(-\frac{t}{\tau_1}\right) + A_2 \exp\left(-\frac{t}{\tau_2}\right), \tag{7}$$

where A_1 and A_2 are the fitted amplitudes, and τ_1 and τ_2 are the characteristic relaxation times of the two relaxation modes. Before $t = 0.1$ ps, $\Delta N_1(t)$ does not change much. This in part is due to the limited energy range of the measurement ($E < E_i = 20$ meV, $h/E_i = 0.2$ ps) so that changes below 0.2 ps cannot be fully resolved. This is the main reason why $A_1 + A_2$ is more than unity. After $t = 1.5$ ps, the data points deviate from the fit. These are artifacts introduced by the overcorrection of energy resolution at long times, especially for low temperatures, because $R(t)$ goes to zero quickly after 1.5 ps. Although imperfect, the energy resolution correction technique is still necessary to obtain more realistic relaxation times. Therefore, only the data from 0.1 to 1.5 ps were used for the two-part exponential decay function fitting, as shown in Fig. 5(a) for $Zr_{50}Cu_{50}$. The determined relaxation times of the two relaxation modes, τ_1 and τ_2, at different temperatures

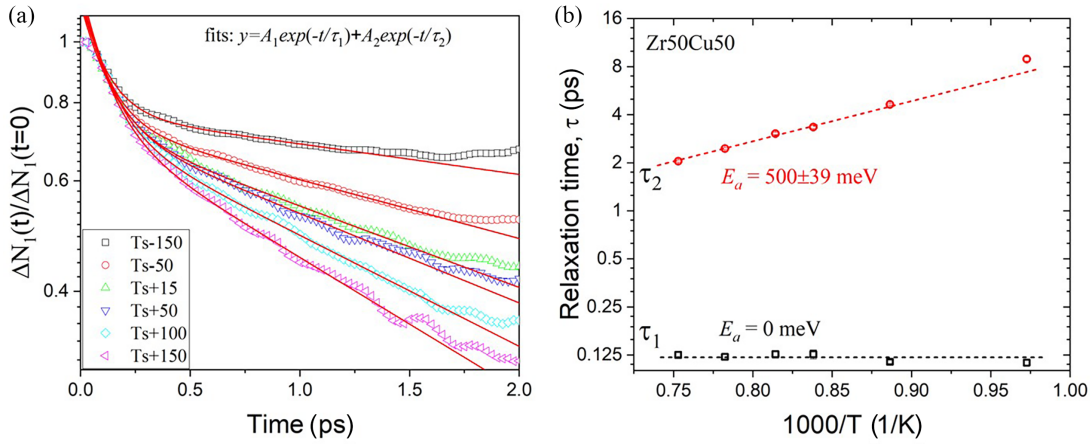

FIG. 5. (a) Normalized $\Delta N_1(t)$ in logarithm scale as a function of time describes the dynamic relaxation in $Zr_{50}Cu_{50}$ liquid at different temperatures. The solid lines are fits to the two-part exponential function from 0.1 to 1.5 ps for the two relaxation modes. (b) The determined characteristic times for two relaxation modes, τ_1 and τ_2, as a function of $1000/T$ for $Zr_{50}Cu_{50}$. The sizes of error bars are smaller than the marker size. The dashed lines indicate the Arrhenius fits and determine the activation energy E_a.

are plotted against the inverse temperature, $1000/T$, as shown in Fig. 5(b) for $Zr_{50}Cu_{50}$ liquid. The error bars from the fitting for most points are smaller than the symbol size.

The apparent activation energies E_a for τ_1 and τ_2 are determined by the Arrhenius equation, $\tau = \tau_0 \exp(E_a/k_B T)$, as shown by the dashed lines in Fig. 5(b). For the faster relaxation mode, τ_1 is small and nearly temperature independent, as expected for a phononic motion of atoms at short times. The value of τ_0 is 0.12 ps, corresponding to 33 meV, which is reasonable for the average phonon energy. For the slower relaxation mode, τ_2 is more strongly temperature dependent with an activation energy of 500 ± 39 meV and $\tau_0 = 0.026$ ps for $Zr_{50}Cu_{50}$. This value of τ_0 is in very good agreement with that for $Zr_{56}Cu_{44}$ obtained by MD simulation for the relaxation time for local configurational excitation, τ_{LC} [11]. Therefore, the τ_2 mode most likely describes changes in local atomic configuration by cutting and forming atomic bonds. The results show that τ_2 follows the Arrhenius law, even at temperatures below T_A, whereas τ_M becomes super-Arrhenius.

It is also noted that E_a for τ_2 determined in this work is about two to three times that determined from the MD simulation in Ref. [11]. This suggests that there may be problems with the classical MD simulation at high temperatures and demonstrates the significance of this study through inelastic neutron scattering experiment. For the $Zr_{80}Pt_{20}$ liquid, similar results were obtained with just longer τ_1 and τ_2 values, and E_a is 47 ± 41 meV for τ_1 and 641 ± 50 meV for τ_2, indicating a slower relaxation and larger energy barrier for the correlated dynamics in $Zr_{80}Pt_{20}$ than that in $Zr_{50}Cu_{50}$. The E_a value of 641 ± 50 meV is slightly different from that in Ref. [12] (750 ± 90 meV for τ_{VH} in $Zr_{80}Pt_{20}$), mainly because of the different fitting ranges to obtain the activation energy.

IV. DISCUSSION

The τ_2 is the relaxation time for the slow relaxation mode of $\Delta N_1(t)$, which depicts the collective motions or correlated dynamics of atoms in the first neighboring shell. Reference [11] introduced τ_{LC}, which is the lifetime of the local atomic connectivity change based on atomic bond cutting and reforming, i.e., the time for a center atom to lose an existing neighboring atom or gain a new one. Therefore, they are directly related to each other. Although τ_{LC} is a definition from MD simulation and cannot be directly measured through experiment, it can be estimated from the experimentally obtained τ_2. Based on the MD simulation results [12,35], τ_2 is about $(4.1–4.4)\tau_{LC}$ for the Fe liquids and about $3.7\tau_{LC}$ for the $Zr_{80}Pt_{20}$ liquid. This relation is reasonable for the metallic liquids as τ_2 indicates the timescale of multiple bond cutting or forming and τ_{LC} indicates the timescale of only one bond cutting or forming. We assume that this relationship still holds for the experimental results in this work, and τ_{LC} can be calculated from the experimentally determined values of τ_2. As shown above τ_2 follows the Arrhenius law even at temperatures below T_A, in agreement with the simulation results for τ_{LC} [37].

On the other hand, the Maxwell relaxation time τ_M can be calculated from the shear viscosity η, measured for the metallic liquids at similar temperatures [31], based on the relationship $\tau_M = \eta/G_\infty$, where G_∞ is the high-frequency shear modulus. Based on the shear modulus of $Zr_{50}Cu_{50}$ glass [38] we estimated $G_\infty = 30$ GPa and calculated τ_M. The crossover temperature T_A is ~1280 K for $Zr_{50}Cu_{50}$ [31] and ~1750 K for $Zr_{80}Pt_{20}$ [39]. The τ_{LC} seems to show Arrhenius behavior within the whole experimental temperature range for $Zr_{50}Cu_{50}$, meanwhile τ_M shows Arrhenius behavior above T_A and super-Arrhenius behavior below T_A. Because τ_{LC} is proportional to τ_2, they have the same activation energy. Furthermore, the activation energy for τ_{LC} and τ_M at high temperatures (Arrhenius part) are similar to each other (500 ± 39 meV vs 630 ± 51 meV for $Zr_{50}Cu_{50}$ and 641 ± 50 meV vs 644 ± 8 meV for $Zr_{80}Pt_{20}$). By estimating τ_{LC} through $\tau_2 = 3.7\tau_{LC}$, the ratio of τ_M/τ_{LC} for $Zr_{50}Cu_{50}$ and that for $Zr_{80}Pt_{20}$ as a function of T/T_A are plotted in Fig. 6. At high temperatures above T_A, $\tau_M \approx \tau_{LC}$. Because τ_M is the timescale to describe macroscopic viscous behavior and τ_{LC} is the timescale to describe changes in local atomic connectivity, this equality connects the macroscopic and microscopic behaviors in metallic liquids directly and shows that the topological excitations in the atomic connectivity determine the viscosity at high temperatures [40].

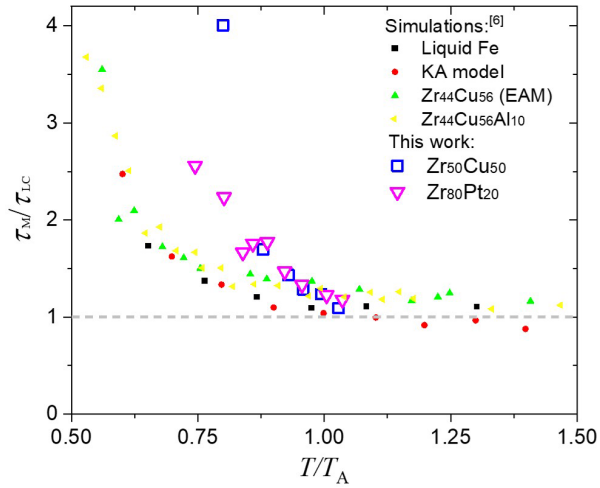

FIG. 6. The ratio of τ_M/τ_{LC} obtained from INS measurements for $Zr_{50}Cu_{50}$ and $Zr_{80}Pt_{20}$ liquids compared with MD simulation results for various metallic liquid models.

At low temperatures below T_A they are no longer equal ($\tau_M > \tau_{LC}$) because atomic dynamics becomes more cooperative. Comparing with the MD simulation results in Ref. [11], it is apparent that they share a very similar trend, although the temperature range measured in INS experiments is much narrower than that of MD simulation, due to limitations like the metallic element evaporation problem, heating capability limit of lasers, and potential crystallization under further deeper supercooling in the levitator. It is also noted that the ratio of τ_M/τ_{LC} for simulated liquid systems increases more slowly with decreasing temperature than the experimentally determined value. This is quite reasonable because the model liquid in MD simulation is cooled much more rapidly than in experiments, and deviates from equilibrium at low temperatures. Thus, τ_M is always underestimated at low temperatures. Here, the "low temperature range" indicates T/T_A below ~0.8 where the model glass could not be fully relaxed. Nevertheless, the similarity between the experimental data

and the MD simulation results provides direct experimental support for the claim from MD simulation that the viscosity of metallic liquids is controlled by the local atomic connectivity change at high temperatures above the crossover temperature T_A and deviates from that below T_A due to atomic cooperativity. It also demonstrates the significance of exploring atomic-level dynamics from real space using inelastic neutron scattering.

V. CONCLUSIONS

The time dependent pair correlation function, the Van Hove function, was obtained from inelastic neutron scattering measurements for $Zr_{50}Cu_{50}$ and $Zr_{80}Pt_{20}$ metallic liquids at different temperatures using an electrostatic levitation facility. Analyzing the relaxation behavior of the distinct part of the Van Hove function, $G_d(r, t)$, the time for local connectivity change τ_{LC} was determined from the experimental data and compared with the Maxwell relaxation time τ_M obtained from the viscosity data. Their equality above the crossover temperature T_A provides the direct experimental evidence for the prediction by MD simulation that viscosity is controlled by the local connectivity change in high temperature metallic liquids. The results also experimentally demonstrate that the atomic dynamics becomes more cooperative below T_A.

ACKNOWLEDGMENTS

The authors thank A. J. Vogt, D. G. Quirinale, and C. E. Pueblo for their help in the neutron scattering experiments. This work was supported by the U.S. Department of Energy, Office of Science, Basic Energy Sciences, Materials Sciences and Engineering Division. The work at Washington University in St. Louis was partially supported by the National Science Foundation under Grants No. DMR-15-06553 and No. DMR-19-04281 and by the National Aeronautics Space Administration (NASA) under Grant No. NNX16AB52G. This research used resources at the Spallation Neutron Source, a DOE Office of Science User Facility operated by Oak Ridge National Laboratory.

This manuscript has been authored by UT-Battelle, LLC under Contract No. DE-AC05-00OR22725 with the U.S. Department of Energy. The U.S. Government retains and the publisher, by accepting the article for publication, acknowledges that the U.S. Government retains a nonexclusive, paid-up, irrevocable, world-wide license to publish or reproduce the published form of this manuscript, or allow others to do so, for U.S. Government purposes. The Department of Energy will provide public access to these results of federally sponsored research in accordance with the DOE Public Access Plan [41].

[1] P. A. Egelstaff, *An Introduction to the Liquid State*, 2nd ed. (Oxford Science Publications, Clarendon Press, New York, 1994).

[2] C. A. Croxton, *Liquid State Physics—A Statistical Mechanical Introduction* (Cambridge University Press, Cambridge, UK, 1974).

[3] J.-P. Hansen and I. R. McDonald, *Theory of Simple Liquids*, 3rd ed. (Academic Press, Amsterdam, 2006).

[4] C. A. Angell, Formation of glasses from liquids and biopolymers, Science **267**, 1924 (1995).

[5] C. A. Angell, K. L. Ngai, G. B. McKenna, P. F. McMillan, and S. W. Martin, Relaxation in glassforming liquids and amorphous solids, J. Appl. Phys. **88**, 3113 (2000).

[6] C. A. Angell, Spectroscopy simulation and scattering, and the medium range order problem in glass, J. Non-Cryst. Solids **73**, 1 (1985).

[7] P. G. Debenedetti and F. H. Stillinger, Supercooled liquids and the glass transition, Nature (London) **410**, 259 (2001).

[8] V. Lubchenko and P. G. Wolynes, Theory of structural glasses and supercooled liquids, Annu. Rev. Phys. Chem. **58**, 235 (2007).

[9] W. Götze, *Complex Dynamics of Glass-forming Liquids* (Oxford University Press, Oxford, 2009).

[10] C. W. Ryu, W. Dmowski, K. F. Kelton, G. W. Lee, E. S. Park, J. R. Morris, and T. Egami, Curie-Weiss behavior of liquids structure and ideal glass state, Sci. Rep. **9**, 18579 (2019).

[11] T. Iwashita, D. M. Nicholson, and T. Egami, Elementary excitations and crossover phenomenon in liquids, Phys. Rev. Lett. **110**, 205504 (2013).

[12] R. Ashcraft, Z. Wang, D. L. Abernathy, D. G. Quirinale, T. Egami, and K. F. Kelton, Experimental determination of the temperature-dependent Van Hove function in a $Zr_{80}Pt_{20}$ liquid, J. Chem. Phys. **152**, 074506 (2020).

[13] L. Van Hove, Correlations in space and time and Born approximation scattering in systems of interacting particles, Phys. Rev. **95**, 249 (1954).

[14] B. N. Brockhouse and N. K. Pope, Time-dependent pair correlations in liquid lead, Phys. Rev. Lett. **3**, 259 (1959).

[15] J. R. D. Copley and J. M. Rowe, Density fluctuations in liquid rubidium. I. Neutron-scattering measurements, Phys. Rev. A **9**, 1656 (1974).

[16] U. Dahlborg, W. Gudowski, and M. Davidovic, Van Hove correlation functions from coherent neutron inelastic scattering, J. Phys.: Condens. Matter **1**, 6173 (1989).

[17] A. Rahman, Density fluctuations in liquid rubidium. II. Molecular-dynamics calculations, Phys. Rev. A **9**, 1667 (1974).

[18] J. Horbach, S. K. Das, A. Griesche, M. P. Macht, G. Frohberg, and A. Meyer, Self-diffusion and interdiffusion in $Al_{80}Ni_{20}$ Melts: Simulation and experiment, Phys. Rev. B **75**, 174304 (2007).

[19] W. Kob and H. C. Andersen, Testing mode-coupling theory for a supercooled binary Lennard-Jones mixture I: The van Hove correlation function, Phys. Rev. E **51**, 4626 (1995).

[20] W. Kob, C. Donati, S. J. Plimpton, P. H. Poole, and S. C. Glotzer, Dynamical heterogeneities in a supercooled Lennard-Jones liquid, Phys. Rev. Lett. **79**, 2827 (1997).

[21] D. S. Simmons and J. F. Douglas, Nature and interrelations of fast dynamic properties in a coarse-grained glass-forming polymer melt, Soft Matter **7**, 11010 (2011).

[22] A. Jaiswal, T. Egami, and Y. Zhang, Atomic-scale dynamics of a model glass-forming metallic liquid: Dynamical crossover,

dynamical decoupling, and dynamical clustering, Phys. Rev. B **91**, 134204 (2015).

[23] T. E. Mason, D. Abernathy, I. Anderson, J. Ankner, T. Egami, G. Ehlers, A. Ekkebus, G. Granroth, M. Hagen, K. Herwig *et al.*, The spallation neutron source in oak ridge: A powerful tool for materials research, Phys. B (Amsterdam, Neth.) **385** 955 (2006).

[24] A. Q. R. Baron, *Synchrotron Light Sources and Free-Electron Lasers* (Springer International Publishing, Cham, 2015).

[25] T. Iwashita, B. Wu, W.-R. Chen, S. Tsutsui, A. Q. R. Baron, and T. Egami, Seeing real-space dynamics of liquid water through inelastic x-ray scattering, Sci. Adv. **3**, 1603079 (2017).

[26] Y. Shinohara, W. Dmowski, T. Iwashita, B. Wu, D. Ishikawa, A. Q. R. Baron, and T. Egami, Viscosity and real-space molecular motion of water: Observation with inelastic x-ray scattering, Phys. Rev. E **98**, 022604 (2018).

[27] Y. Shinohara, R. Matsumoto, M. W. Thompson, C. W. Ryu, W. Dmowski, T. Iwashita, D. Ishikawa, A. Q. R. Baron, P. T. Cummings, and T. Egami, Identifying water-anion correlated motion in aqueous solutions through Van Hove functions, J. Phys. Chem. Lett. **10**, 7119 (2019).

[28] T. Kordel, D. Holland-Moritz, F. Yang, J. Peters, T. Unruh, T. Hansen, and A. Meyer, Neutron scattering experiments on liquid droplets using electrostatic levitation, Phys. Rev. B **83**, 104205 (2011).

[29] D. L. Abernathy, M. B. Stone, M. J. Loguillo, M. S. Lucas, O. Delaire, X. Tang, J. Y. Y. Lin, and B. Fultz, Design and operation of the wide angular-range chopper spectrometer ARCS at the Spallation Neutron Source, Rev. Sci. Instrum. **83**, 015114 (2012).

[30] N. A. Mauro, A. J. Vogt, K. S. Derendorf, M. L. Johnson, G. E. Rustan, D. G. Quirinale, A. Kreyssig, K. A. Lokshin, J. C. Neuefeind, K. An *et al.*, Electrostatic levitation facility optimized for neutron diffraction studies of high temperature liquids at a spallation neutron source, Rev. Sci. Instrum. **87**, 013904 (2016).

[31] M. E. Blodgett, T. Egami, Z. Nussinov, and K. F. Kelton, Proposal for universality in the viscosity of metallic liquids, Sci. Rep. **5**, 13837 (2015).

[32] R. T. Azuah, L. R. Kneller, Y. Qiu, P. L. Tregenna-Piggott, C. M. Brown, J. R. Copley, and R. M. Dimeo, DAVE: A comprehensive software suite for the reduction, visualization, and analysis of low energy neutron spectroscopic data, J. Res. Natl. Inst. Stand. Technol. **114**, 341 (2009).

[33] O. Arnold, J. C. Bilheux, J. M. Borreguero, A. Buts, S. I. Campbell, L. Chapon, M. Doucet, N. Draper, R. Ferraz Leal, M. A. Gigg *et al.*, Mantid–Data analysis and visualization package for neutron scattering and μ SR experiments, Nucl. Instrum. Methods Phys. Res., Sect. A **764**, 156 (2014).

[34] G. L. Squires, *Introduction to the Theory of Thermal Neutron Scattering* (Cambridge University Press, Cambridge, UK, 2012).

[35] B. Wu, T. Iwashita, and T. Egami, Atomic dynamics in simple Liquid: De gennes narrowing revisited, Phys. Rev. Lett. **120**, 135502 (2018).

[36] T. Egami and S. Aur, Local atomic structure of amorphous and crystalline Alloys: Computer simulation, J. Non-Cryst. Solids **89**, 60 (1987).

[37] T. Iwashita and T. Egami, Local energy landscape in a simple liquid, Phys. Rev. E **90**, 052307 (2014).

[38] W. H. Wang, Correlations between elastic moduli and properties in bulk metallic glasses, J. Appl. Phys. **99**, 093506 (2006).

[39] Value of T_A reexamined by K. F. Kelton (private communication).

[40] T. Egami, Elementary excitation and energy landscape in simple liquids, Mod. Phys. Lett. B **28**, 1430006 (2014).

[41] http://energy.gov/downloads/doe-public-access-plan.